Hydrogen ions (H^+) implantation induced interstitial defects for performance enhancement of flexible dye-sensitized solar cells (FDSSCS)

Ikram-ul-Haq[a,*], M. I. Khan[a], M. Irfan[a], M. Usman[b], S. Ul Hasan[c], Imtiaz Ahmad[d], Ihab Mohamed Moussa[e]
[a]*Department of Physics, The University of Lahore, 53700, Pakistan*
[b]*National Center for Physics, Islamabad, Pakistan*
[c]*Institute of Functional Nano & Soft Materials (FUNSOM), Jiangsu Key Laboratory for Carbon-Based Functional Materials & Devices, Soochow University, Suzhou, People's Republic of China*
[d]*Department of Physics and Astronomy, Texas Tech University, Lubbock, TX 79409, USA*
[e]*Department of Botany and Microbiology, College of Science, King Saud University, P.O. Box 2455, Riyadh, 11451, Saudi Arabia*

To enhance the performance of flexible dye-sensitized solar cells (FDSSCs), zinc oxide (ZnO) powder is prepared using the hydrothermal method and spin-coated onto plastic substrates. The films are implanted with H^+ ions at three fluencies (1×10^{13}, 1×10^{14}, and 1×10^{15} ions/cm^2). XRD results reveal the hexagonal (wurtzite) structure with improved crystallinity. SRIM software analyzed that with an increasing ion dose, vacancies are increased. UV-Vis shows increased bandgap energy. PL confirms reduced recombination rates. Photovoltaic measurements of FDSSCs demonstrate significantly enhanced efficiency (2.86%) at 1×10^{14} ions/cm^2 fluence. EIS confirms the suppression of charge recombination and reduced charge transport resistance.

(Received July 1, 2024; Accepted September 16, 2024)

Keywords: ZnO electrodes, FDSSCs, DSSCs, Solar cells

1. Introduction

FDSSCs have become an appealing replacement for traditional silicon-based solar devices due to their affordable price, easy and quick fabrication, and potential for flexibility [1]. Traditional rigid substrates, such as glass or FTO, limit the flexibility and practicality of DSSCs. Thus, developing flexible photoanodes is of great importance for realizing the full potential of DSSCs in flexible and portable electronics. The FDSSCs have important components, including a photoanode, sensitizer, mediator, counter electrode, and substrate [2]. Among these, photoanode is crucial in light absorption and charge transport [3, 4]. Researchers have used various wide-band materials as photoelectrodes in FDSSCs which include SnO_2 [5], ZnO [6], and TiO_2 [7]. These mentioned semiconductors offer favorable optoelectronic properties and have been extensively studied for their potential to enhance the performance of FDSSCs. Due to its remarkable properties, ZnO has been increasingly studied as a photoanode for FDSSCs in recent years. These properties include that ZnO has different morphologies like nanorods, nanoflowers, nanotubes, and nanowires [8]. It has a higher electron mobility than TiO_2 [9], a larger bandgap (3.37 eV), 60 meV excitons binding energy, high charge carrier concentration, excellent optical transparency, and a conductivity span of 10^4 to 10^{-12} Ωcm [10]. Excitonic emission, nontoxicity, the quantum confinement effect, and good transparency within the visible spectrum associated with ZnO contribute to its potential for use in diverse fields, including solar cells, optoelectronics, and sensors. These superior characteristics make ZnO a desirable candidate for utilization in FDSSCs, enabling efficient light absorption, charge separation, and electron transport processes [11, 12]. However, several challenges still need to be addressed to improve the efficiency and flexibility of

* Corresponding author: ikrmhaq@gmail.com
https://doi.org/10.15251/JOR.2024.205.633

FDSSCs based on ZnO. The quick electron-hole pairs recombination, which lowers the overall device performance, is one of the fundamental constraints of ZnO-based FDSSCs. The other limitation is the disintegration of ZnO into Zn^{2+} ions due to acidic sensitizers adsorbed onto its surface and the formation of dye aggregates, adversely affecting ZnO's performance as a photoanode in FDSSCs. This corrosion and reduced efficacy in an acidic atmosphere impose limitations on utilizing ZnO as a photoanode material in FDSSCs [13]. Various strategies have been explored to eliminate the issue, including surface modifications, nanostructuring, doping, and ion implantation. Ion beam implantation is a powerful technique to modify micro to nanoscale material properties. Researchers can precisely alter the characteristics of ZnO thin films by controlling ion density, creating defects, and inducing stress/strain [14]. This unique method offers promising technological applications and is acknowledged as an effective tool for tailoring material properties [15, 16]. ZnO can be modified by introducing foreign dopants, such as In, B, Mg, Mn, H, Al, Ga, Li, N, C, S, Se, etc., to achieve desired properties. These impurities enable the alteration of the band structure, the creation of imperfections, and improvement in the mobility of charge carriers in ZnO [17].

ZnO-photoelectrode fabrication with p-type characteristics can be produced by replacing Zn with elements of group I [18] or O with elements of group V from the ZnO lattice [19]. It is better to achieve the p-type behavior of ZnO by incorporation of elements from group I than from group V as they can develop shallow acceptor levels in the ZnO lattice [20]. Thus the implantation of the elements from group–I can improve the various features of the p-type ZnO photoelectrodes for FDSSCs. The close resemblance in size is a very important factor as it can enable the easy substitution of group-I ions with Zn^{2+} ions to induce p-type conductivity within the crystal lattice of ZnO [21].

Hydrogen ions (H^+) implantation has emerged as a promising technique to enhance the performance of ZnO-based photoanodes. H^+-implantation has been shown to effectively passivate surface defects and suppress electron-hole recombination in ZnO, leading to improved charge separation and transport. Moreover, H^+-implantation offers the advantage of being a low-cost, scalable, and environment-friendly process. Chris et al. reported that the incorporation of hydrogen (H) ions in ZnO is known to enhance conductivity. H ions, being stable and existing in the lowest-energy state across all Fermi-level positions, can be incorporated in significant concentrations as shallow donors in ZnO. This results in improved conductivity properties for ZnO-based materials [22]. Kim et al. treated the H ions in ZnO film and reported that it reduced the electron trap sites and electron scattering which improved the performance of the film [23]. Hoang et al. have reported that H atoms located at oxygen vacancy sites (H_O) play a crucial role in simultaneously increasing the mobility and carrier concentration of ZnO. The presence of H_O defects caused by hydrogen is a significant contributing factor to the observed enhancements in both mobility and carrier concentration [24]. Myong et al. reported that H incorporation in ZnO improves the carrier concentration, and electron transportation and reduces the trap sites [2].

The current study delves into pioneering research that revolves around the fabrication and meticulous characterization of H^+-implanted ZnO-based photoanodes specifically tailored for FDSSCs. Notably, this investigation employs an innovative approach by utilizing indium tin oxide laminated polyethylene terephthalate (ITO-PET) flexible substrates, emphasizing the pursuit of flexibility and adaptability in solar cell technology. The primary objective encompasses a comprehensive examination of the influence of H+-implantation on various facets of ZnO films. The structural, morphological, optical, and impedance properties of these films are meticulously scrutinized, shedding light on the profound modifications induced by the implantation process. This thorough analysis aims to uncover the nuanced changes and enhancements in ZnO's characteristics, crucial for optimizing its performance as a photoanode in FDSSCs. Moreover, the research meticulously evaluates the photovoltaic parameters, elucidating the direct impact of these structural and property modifications on the overall efficacy and efficiency of FDSSCs. By correlating these findings, the study intends to establish a comprehensive understanding of how H^+-implantation influences the performance of ZnO-based photoanodes within the context of flexible dye-sensitized solar cells. This novel approach holds significant promise in advancing the frontier of solar cell technology toward enhanced flexibility, efficiency, and practicality.

2. Experimental arrangement

2.1. Materials and methods

A uniform blend of zinc oxide (ZnO) was prepared using the hydrothermal method. In this process, the first solution is prepared by mixing 1M of $(Zn\,(CH3COO)_2\,.2H_2O$ with 0.5M HMTA. Then the 1M of sodium hydroxide (NaOH) is slowly poured into the first solution while continuously stirring. The solution was magnetically stirred at above 7 PH for approximately four hours to ensure homogeneity. The resulting mixture was shifted to a Teflon-lined autoclave, filled to 85% capacity, at 100 °C for 36 hours. Afterward, the autoclave was left to cool to a normal temperature. The white slurry blend was filtered, cleaned with ethanol and distilled water, dried, and crushed into powder. This powder was then mixed in ethanol, and a uniform ZnO mixture was prepared after sonification. The mixture was then applied to the (ITO-PET) plastic substrates using the spin coating method to develop ZnO films that were subsequently placed under heating at 80 °C for 45 minutes. The four films were synthesized, including one as the referenced film symbolized by HZnO-0. The next three films were irradiated with H^+ ions at three fluencies: 1×10^{13}, 1×10^{14}, 1×10^{15} ions/cm^2 and termed as (HZnO-1), (HZnO-2), and (HZnO-3) respectively. The H^+-implanted ZnO films can be collectively denoted as (HZnOs). The implantation was carried out using an Accelerator (Palletron) with 700 keV energy.

2.2. Characterization techniques

For structural analysis of the ZnO-based photoelectrodes, an X-ray diffractometer (XRD) (Proto Model: AXRD Benchtop, Canada) was used. The amounts of ionization and vacancies produced due to these interactions in ZnO have been estimated by using Stopping and Range of Ions in Matter (SRIM) software. The morphologies of the films were discovered via a scanning electron microscope (SEM) (Nova Nano SEM 450 FEI), operating at 1 nm at 1 kV (TLD-SE) and 1 nm at 16 kV (TLD-SE). The films' spectral behavior was evaluated using a UV-Vis spectrophotometer (Shimadzu| Model: UV 3600 plus| Origin: Japan). With the use of a photoluminescence (PL) spectrophotometer (Fluromax4, Horiba, USA), the trap levels were studied. The electrochemical impedance was analyzed by impedance spectrometer (CHI660E) under conditions (V= 10 mV, f= 100 mHz-10 kHz).

2.3. Fabrication of FDSSCs

To develop FDSSCs, the as-produced ZnO electrodes were immersed in a 0.3 mM N719 sensitizer solution for 36 hours. The dye-loaded electrodes were washed with ethanol or distilled water and then left to dry in an oven for 36 hours. The construction of the FDSSCs was completed by introducing an iodine electrolyte ($3I^-/I_3^-$) at the interface of photoelectrode/platinum (Pt) counter electrode (CE). For the evaluation of the performance of these devices, a source meter of model Keithley 2450 with 1.5G sun simulator light at 100 mWcm^{-2} was used. Figure 1 illustrates the function of FDSSCs that is given below.

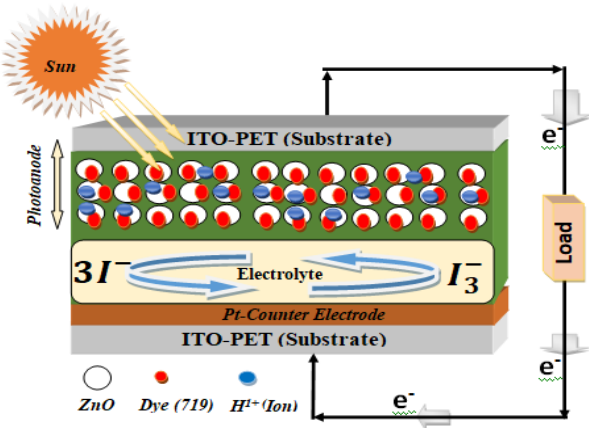

Fig. 1. Schematic diagram of FDSSCs.

3. Results and discussions

3.1. XRD analysis

The ZnO films were investigated through structural analysis via X-ray diffraction (XRD). The results and detailed information regarding the crystal structure and plane orientation are presented in Figure 2. The Miller Indices (hkl) nomenclature was used to describe the plane orientations of the ZnO crystal structure.

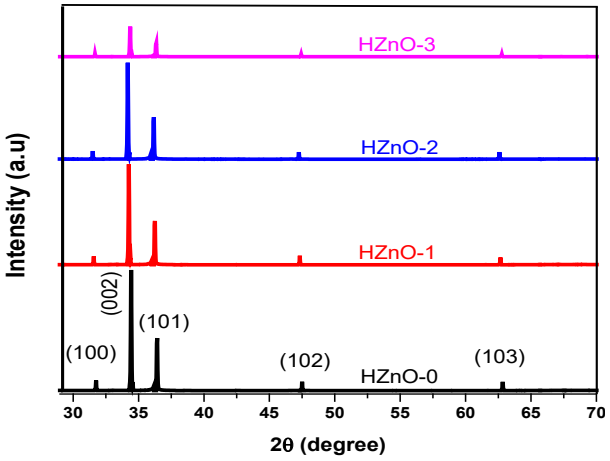

Fig. 2. The XRD images for ZnO and HZnO films.

The important peaks that appeared in the XRD spectra are (100), (002), (101), (102), and (103). All the peaks for unimplanted (HZnO-0) are observed at 31.78°, 34.46°, 36.38°, and 62.83° respectively. The (002) peak has the highest intensity out of all the peaks. The (002) peaks corresponding to H^+-implanted ZnO films (HZnO-1, HZnO-2, HZnO-3) are positioned at 34.45°, 31.41°, and 31.43° respectively. The films bear a hexagonal (wurtzite) structure, whether implanted or not, comparable to the JCPDS card number (00–036-1451) [25]. Compared to unimplanted films, no secondary or extra phases appear in the H^+-implanted films (HZnOs).

The irradiation of the H^+ ions into the ZnO lattice for fluency $1 \times 10^{13}\ ions/cm^2$ decreases the intensity of the peak (002) showing a decrease in the crystallinity of the films. The (002) peak intensity decreases on increasing the H^+ ion dose, representing that crystallite alignment along the c-axis decreases on increasing the ion dose. It is also observed that 2θ shifts towards a lower angle by amounts 0.01°, 0.05°, and 0.03° for the films HZnO-1, HZnO-2, HZnO-3 respectively. According to Bragg's Law, the unit cell size can shrink if the peak is broadened, which may be because the foreign H^+ ion has made an acceptor interstitial position in the ZnO lattice. In ion implantation, it is essential to consider the size of the implanted ion; if the ion has a very small size then during implantation it can induce interstitial defects in the lattice (ZnO). As the size of H^+ is very small as compared to Zn^{2+}, the interstitial defects are most probable. In the interstitial defects, H^+ occupies the interstitial sites within the ZnO lattice [26]. Consequently, the lattice disrupts and peak intensity decreases with 2θ angle shifts towards lower values [9, 27, 28]. The literature also reported that if an ion from group-I element is incorporated in ZnO, peak intensity decreases and 2θ may shift towards the lower angle [27]. In comparison to HZnO-1 and H-ZnO-2, the film (HZnO-3), which is implanted at a heavy fluency of 1×10^{15} ions/cm^{2,} shows a relatively large distortion because at a heavy ion dose the lattice degraded in crystallinity [29]. Peak shifting and decrease in the intensity of (002) peak indicate that the H^+ ion is successfully interstitially occupied in the ZnO lattice [30].

The crystallite size (average) denoted by (D) and dislocation line density (DLD) (δ) along the (002) plane were determined using the Debye-Scherrer relation, and the measurements are tabulated in Table 1 [31].

$$D = \frac{k\lambda}{\beta cos\theta} \quad (1)$$

$$\delta = \frac{1}{D^2} \quad (2)$$

The above relation has k = 0.9 (Scherrer's constant), β = full width at half maximum, (FWHM), θ=Bragg's angle (radians), and $\lambda = 0.15406\,\text{nm}$ is the wavelength of $\text{Cu} - \text{K}\alpha$ radiation [32].

Implantation of H^+ ions into the ZnO lattice induces changes in the mean crystallite size (D). For instance, when the film is implanted at 1×10^{13}, 1×10^{14}, and 1×10^{15} ions/cm^2, the D values observed are 28, 26, 18, and 20 nm. This decrease in D can be ascribed to the peak broadening caused by the H^+ ions occupying the interstitial site in the ZnO film [33, 34]. The shrinkage in crystallite size offers more surface area for dye loading and thus can generate more charge carriers [35, 36]. The δ is calculated to evaluate the lattice imperfections. The "δ" value suggests decreased film quality if its value is high. The dislocation line density exhibits an increasing trend for all fluences, indicating lower crystal quality.

Bragg's law is considered to calculate the inter-planner spacing [37]:-

$$\mathrm{d} = \frac{\mathrm{n}\lambda}{2\sin\theta} \quad (3)$$

In the above equation, n is an integer representing the diffraction order. In the case of the (002) peak of the ZnO film, the d-spacing is influenced by introducing H^+ ions through ion implantation. The d-spacing values corresponding to the (002) peak for the unimplanted HZnO-0) and implanted films (HZnO-1, HZnO-2, HZnO-3) are 2.28, 2.32, 2.43, and 2.38 Å. It is seen that the d-spacing values corresponding to the (002) peak are increased upon H^+ ions implantation. These changes in d-spacing can be attributed to the implantation of H^+ that interstitially occupied the ZnO lattice and caused it to expand. The measured d-spacing values align closely with the PDF card numbers (36-1451) for ZnO having a hexagonal (wurtzite) structure [38].

The following expressions measure the lattice constants of all the films [39].

$$\frac{1}{\mathrm{d}_{\mathrm{hkl}}^2} = \frac{4}{3}\left(\frac{\mathrm{h}^2+\mathrm{hk}+\mathrm{k}^2}{\mathrm{a}^2}\right) + \frac{\mathrm{l}^2}{\mathrm{c}^2} \quad (4)$$

This relation allows us to understand how the implantation process influences the lattice parameters of ZnO films [40]. By varying the implantation conditions, such as ion dose and energy, we can observe changes in the lattice parameters of the films [41]. These changes provide insights into the structural modifications occurring within the ZnO lattice due to the implantation of foreign ions. The values of (a, b, c) parameters for the prominent peak (002) of all the films were determined using (hkl) indices and are presented in Table 1. These results indicate the crystalline nature of the ZnO films. Upon implantation of H^+ ions into the ZnO film, an increment in the lattice parameters (a, c, d) was observed and can be ascribed to the interstitial occupation of H^+ ions that influence the extension of lattice and lattice parameters [42]. Additionally, variations in lattice strains, subsequently impact the lattice and optical properties [43, 44].

The following formula can measure the surface volume (V) [45].

$$V = (0.866 \times a^2 \times c) \quad (5)$$

The surface volume of the films HZnO-0, HZnO-1, HZnO-2, and HZnO-3 have values of 48.58 (Å)^3, 48.60 (Å)^3, 48.66 (Å)^3, and 48.62 (Å)^3, respectively. In comparison to unimplanted ZnO films, the H^+-implanted ZnO films lead to an increase in surface volume which is due to the introduction of H^+ ions that increase in surface volume [36, 46].

Strains have a significant role in investigating the H^+ ions implantation-related modifications in the ZnO lattice. The following equations determine the strains associated with the prominent peak (002) of all the films [44, 47]:

$$\varepsilon_{zz} = \frac{c-c_0}{c_0} \times 100\% \quad (6)$$

$$\varepsilon_{xx} = \frac{a-a_0}{a_0} \times 100\% \quad (7)$$

The notations ε_{zz} and ε_{xx} represent the c-axis strains and a-axis strains, respectively. Upon H^+ implantation into the ZnO lattice, the ε_{zz} and ε_{xx} exhibit an increasing trend. These variations in strains are ascribed to the H^+ ion implantation into the ZnO lattice. Further details regarding the XRD features can be found in Table 1.

Table 1. XRD parameters of all the films.

Sample	***D*** **(nm)**	**δ** **(10^{-4}m^{-2})**	**d** (Å)	***c***(Å)	***a***(Å)	***c/a***	***V*** ***(Å)³***	ε_{zz} ***(a.u)***	ε_{xx} ***(a.u)***
HZnO-0	32	9.77	2.28	*3.270*	5.258	1.608	48.68	0.99	0.64
HZnO-1	28	12.8	2.32	*3.275*	5.265	1.608	48.90	1.13	0.80
HZnO-2	20	25.0	2.43	*3.290*	5.290	1.608	49.59	1.61	1.26
HZnO-3	22	20.7	2.38	*3.280*	5.275	1.608	49.15	1.33	0.95

3.2. Simulations through SRIM software

The Stopping and Range of Ions in Matter (SRIM) software has anticipated that the energetic H^+ ions produce defects in the ZnO films due to the interaction with the target material through electronic and nuclear scattering processing. The electronic interactions produce ionization in the ZnO whereas the nuclear interactions produce defects in the lattice structure through nuclear stopping producing defects around the projected range of incident H^+ ions. The amounts of ionization and vacancies produced due to these interactions in ZnO have been estimated by using SRIM software. Figure 3 (a & b) shows the obtained results from the simulations for ionization and vacancies produced in the ZnO with direct interactions as well as recoils. It is to mention that each ion produces ~15 average vacancies in ZnO and the projected H^+ ion's range is 5.6 µm.

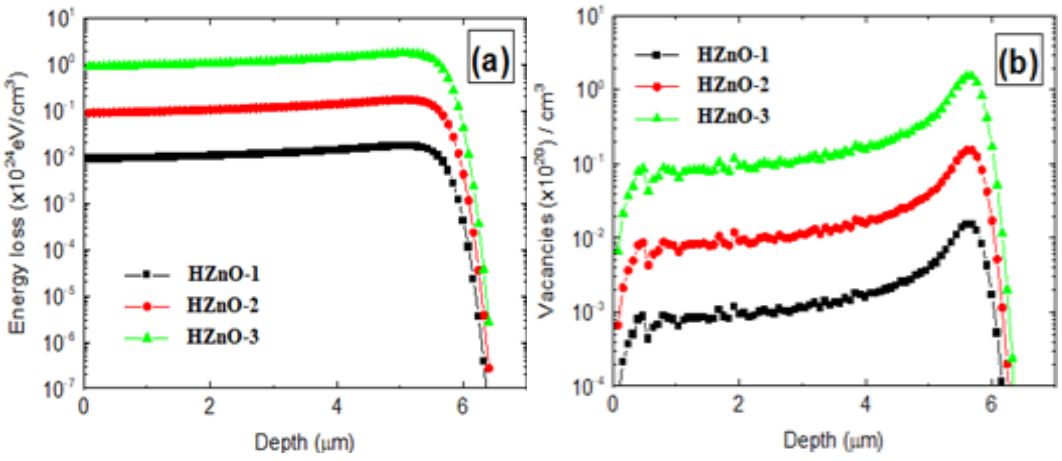

Fig. 3. (a) Ionization, (b) Vacancies produced in HZnOs films.

3.3. SEM analysis

SEM studies evaluate the materials' morphology, as Figure 3 (a-d) illustrates. The proper implantation of H^+ into ZnO films is observed in the SEM micrographs. The SEM images show the fluence-dependent impact of the H^+ ions on the ZnO lattice. This effect arises due to different small sizes of H^+. It is found that by increasing the implantation dose of H^+ ions, the layers become more porous and have rougher surfaces, enhancing its dye adsorption and improving the light-harvesting performance. In this respect, HZnO-2 film implanted at the fluence 1×10^{14} ions/cm^2 is more porous than the other films; therefore, it can adsorb more dye than the rest of the films and thus produce more excited electrons and increase the current density. No more impurities are discovered in the H^+-implanted ZnO films, which show the compound's purity.

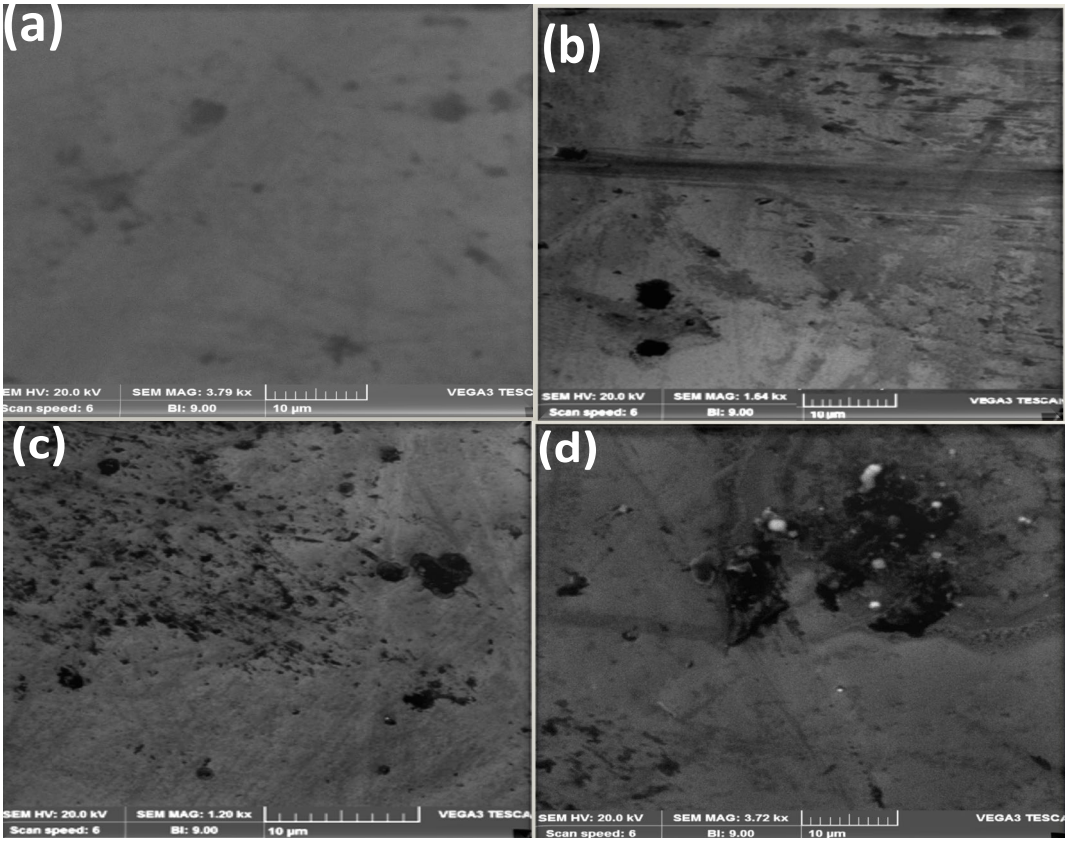

Fig. 4. The SEM images of unimplanted and the H-implanted ZnO films (a, b, c, d).

3.4. UV-visible investigations

The UV-visible investigations were employed to characterize unimplanted and H^+-implanted ZnO films. These measurements were conducted at standard temperatures within the wavelength span of 280 nm to 750 nm. The UV-Vis absorbance spectra are presented in Figure 4a.

The ZnO films exhibit absorption of UV radiation, facilitating electronic transitions from the valence band (VB) to the conduction band (CB). The absorptional characteristics of ZnO films are modified by introducing H^+-ions into the lattice. Compared to unimplanted film, the H^+-implanted films display an increase in absorbance. Upon H^+ ions implantation into the ZnO lattice, absorption edges are blue-shifted due to the material's electronic structure modifications caused by oxygen vacancies and Zn-interstitial sub-bands. These alterations contribute to modifications to improve the optical properties. The reduced absorbance observed in H^+-implanted films indicates the potential for improving the transparency of light reaching to dye for enhancing the production of charge carriers. It highlights the significance of H^+-ion implantation in modifying the optical behavior of ZnO films.

Upon H^+-ions implantation, the absorbance of the films decreases for HZnO-1 and HZnO-2, except for HZnO-3 implanted at 1×10^{15} ions/cm^2 high fluence. All the films demonstrate effective absorption of UV radiation from 255 nm to 325 nm wavelength range. However, the absorbance gradually decreases beyond this range and becomes negligible for wavelengths exceeding 430 nm [48]. The sharp absorbance peaks in the ZnO film signify the efficient stimulation of charge carriers from the VB to the CB, encompassing broad wavelength spectra. As the H^+-implantation dose increases, the absorption edges are reduced, suggesting a possible bandgap widens. This observation highlights the tunability of ZnO films through H^+-ions implantation that requires tailored band gaps [49]. Among the other films, the H^+-(1×10^{14} ions/cm^2)-ZnO film exhibits the highest transmittance within the visible spectrum range. As a result, more photons are transmitted from the semiconductor material to the dye. The increased photon absorption generates a more significant number of charge carriers, ultimately enhancing solar cells' current density and performance.

Tauc's plot, depicted in Figure 4b, measures the bandgap (E_g) of the films [50].

$$\alpha h\nu = A\,(h\nu - Eg)^n \tag{8}$$

The following relation can measure the absorption coefficient (α) [51, 52].

$$\alpha = \frac{2.303A}{t} \tag{9}$$

These equations involve variables like the absorption coefficient (α), bandgap energy (Eg), incident photonic energy (hν), and a constant (A). It is important to note that in direct bandgap materials, the value of "n" is considered a half-integral (½). In contrast, for indirect bandgap materials, it is equal to 2 [53] [54].

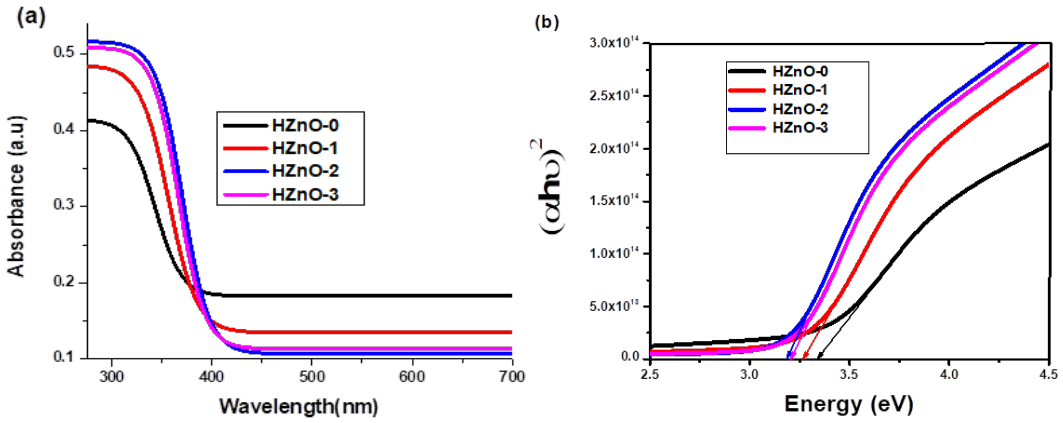

Fig. 5. (a) Showing the absorbance curve of all the films and (b) showing bandgaps of all the films.

The unimplanted and H^+ implanted ZnO films have a bandgap of 3.335 eV, 3.266 eV, 3.200 eV, and 3.214 eV, respectively. The bandgap decreases upon H^+ ions implantation at dosages 1×10^{13} and 1×10^{14} ions/cm^2. The bandgap narrowing can be attributed to the introduction of acceptor H^+ ions at the interstitial sites in the ZnO lattice [55]. The work function of H^+ ions (2.3 eV to 2.9 eV) is different from ZnO (5.4 eV), so when it is implanted into the ZnO lattice, then the fermi level experiences a downward shift nearer to VB [35, 56].

The refractive index measures how light bends in a material. In FDSSCs, the refractive index of the photoanode affects light absorption. Suppose if it is too low, then light escapes without being absorbed. But if it's too high, the light gets trapped, reducing the current generation. Optimizing the refractive index improves FDSSC efficiency. Its measurement follows the relation by Hervé and Vandamme [57]:-

$$n = \sqrt{1 + (\frac{A}{E_g + B})^2} \quad (10)$$

The constants A=13.6 eV and B=3.4 eV are derived from the Lorentz classical theory [58, 59]. The refractive indices, measured at fluencies of 1×10^{13}, 1×10^{14}, and 1×10^{15} ions/cm^2, are 2.253, 2.272, 2.290, and 2.287, respectively. The H^+ ions implantation increases the value of n of the lattice due to enhanced absorbance spectra [60, 61].

The extinction coefficient (k) is a well-known parameter used to quantify the absorption strength of a material at a specific wavelength. It is a fundamental property that determines how efficiently a material absorbs light. In the context of FDSSCs, the k value of the photoanode material is a crucial parameter in achieving the high efficiency of the device. Higher values of k indicate more substantial light absorption capability, allowing for enhanced electron transfer to the semiconductor material. However, it is essential to strike a balance between a high extinction coefficient and high charge injection efficiency. Excessively high values of k can lead to the undesired quenching of excited dye molecules within the photoanode, resulting in reduced charge injection efficiency. Therefore, optimizing the dye and photoanode material extinction coefficients is necessary to ensure the highest possible efficiency in FDSSCs [62].

For the calculation of the extinction coefficient (k) of the films, the formulism is given below [63]:-

$$k = \frac{n}{\triangle\chi^* \gamma} \quad (11)$$

$$Here\ \triangle\chi^* = \frac{E_g}{3.72} \quad (12)$$

The parameter $\Delta\chi^*$ can be obtained by taking the electronegative difference of the cations and anions, where γ (-0.32) is used as a fixed constant. The measured values of k for all the samples are 2.176, 2.179, 2.183, and 2.182 (cm^{-1}). The ZnO films with H^+ implantation have higher k values than those without implantation. Among the H^+-implanted films, the highest k value is observed for the film (HZnO-2) implanted at a dose of 1×10^{14} ions/cm^2. Adding Group-I elements into the ZnO lattice, such as H^+ ions, increases k values [64, 65]. Furthermore, ZnO films implanted with H^+ ions show high absorption in the spectral band where the k values are greater [66]. Optimizing the value of k is beneficial for the performance of FDSSCs as it increases absorption.

The dielectric constant (Ɛ) represents the capacity of a material to store electrical energy within an electric field. In FDSSCs, the photoanode material, typically a porous semiconductor, possesses a high dielectric constant. The real part (ε_r) influences the electric field strength within the material, impacting charge separation and transport. The imaginary part (ε_i) affects charge carrier recombination and cell efficiency [67]. Moreover, the imaginary part is linked to light absorption and scattering in the material. A higher imaginary part enhances light harvesting, while a lower value reduces light scattering and promotes light transmission. According to a certain formulation, the dielectric constant is stated as a combination of its real and imaginary parts [68]:-

$$\varepsilon = \varepsilon_r + i\varepsilon_i \quad (13)$$

$$\varepsilon_r = n^2 - k^2 \quad (14)$$

$$\varepsilon_i = 2nk \quad (15)$$

The energy of photons (hf) plays a significant role in influencing the dielectric constant and its components [69]. The photon energy directly influences the values of these components. The contrast of ε_r and ε_i of the materials' dielectric constant suggests a considerable interaction between photons and electrons. Implantation of H^+ ions increases the dielectric constant, indicating a decrease in the polarization within the material that enhances the mobility of charge carriers and improves current flow [70, 71]. The values of dielectric parts are mentioned in Table 2.

In the realm of FDSSCs, the bandgap edges hold profound importance. They determine the maximum photon energy absorbed, influencing current density and voltage. Precise optimization is crucial for high efficiency. E_{CB} and E_{VB} represent the bandgap edges of CB and VB, respectively, and can be estimated using expressions given below [72]:-

$$X = \frac{1}{2}(E_{EA} + E_{ion}) \tag{16}$$

$$E_{CB} = X - E_C - \frac{1}{2}E_g \tag{17}$$

$$E_{VB} = E_{CB} - E_g \tag{18}$$

The study reveals a notable trend in the bandgap edges as a function of ion doses. At doses of 1×10^{13} and 1×10^{14} ions/cm², a decrease in the bandgap edges is observed. Conversely, at a dose of 1×10^{15} ions/cm², an increase in the bandgap edges is evident. This intriguing behavior suggests a potential bandgap shrinkage phenomenon induced by the ion implantation. Detailed values of the bandgap edges can be found in Table 2, and a graphical representation is provided in Figure 5, offering a visual depiction of these findings.

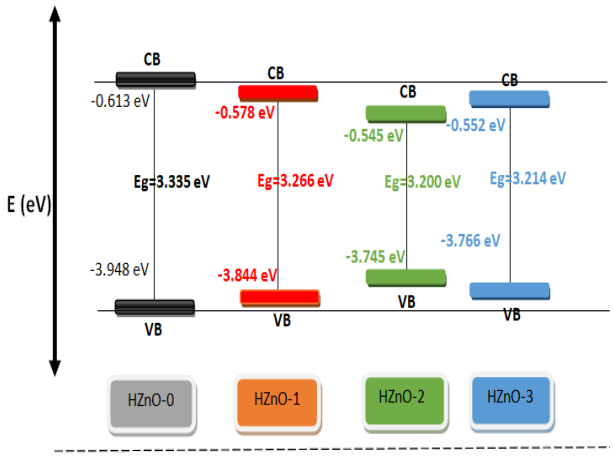

Fig. 6. Bandgap edges of all the films.

Table 2. Optical parameters of all the films.

Samples	Bandgap (E_g)	Refractive Index (n)	Extinction Coefficient (k)	Dielectric Constants		Band Edges	
				ε_r	ε_i	E_{CB}	E_{VB}
HZnO-0	3.335	2.253	2.176	0.155	9.806	-0.613	-3.948
HZnO-1	3.266	2.272	2.179	0.185	9.904	-0.578	-3.844
HZnO-2	3.200	2.290	2.183	0.215	9.999	-0.545	-3.745
HZnO-3	3.214	2.287	2.182	0.209	9.978	-0.552	-3.766

3.5. Photoluminescence (PL) study

Photoluminescence (PL) spectroscopy can be utilized for assessing the efficacy of charge carriers' recombination rates and their transfer process within the photoanode. By exciting the photoanode with the light of a specific wavelength, PL spectroscopy enables the measurement of emitted light intensity and wavelength. This invaluable technique allows for determining energy levels, electronic properties, bandgap, and defects within the material. Moreover, PL

measurements shed light on the surface quality, concentration, and mobility of charge carriers within the photoanode. To investigate the impact of implanted ions, particularly in unimplanted and H^+-implanted ZnO films (HZnOs), photoluminescence (PL) examinations were conducted and are presented in Figure 6. The PL spectra of the ZnO films exhibited distinct peak characteristics encompassing two distinct categories. The first peak type is NBE (near band edge emissions) that appeared in the UV range (360nm-375nm) and corresponded to exciton emissions. These emissions are closely associated with the bandgap transitions. These emissions also explain the acceptor levels demonstrating electron transfers from the interstitial level to the trapped states [73]. The second peak type emerged in the visible spectrum (~550 nm) and stemmed from electron-hole (e-h) recombination triggered by defects of zinc-interstitial or oxygen-vacancies. These emissions, known as deep-level emissions (DLE), are attributed to defect-related processes within the material [74, 75].

All films' ultraviolet (UV) emissions (NBE) were examined, resulting in observed wavelengths of approximately 362 nm, 363 nm, 364 nm, and 363 nm, respectively. A blue-shift emission was observed in the UV peaks of the H^+-implanted ZnO films, possibly due to reduced E_g, as previously reported in the UV-VIS analysis [76]. Green-yellow related emissions were detected at approximately 535 nm, 539 nm, 548 nm, and 541 nm for all the films, attributed to transitions from Zn interstitial to VB [53]. The implantation of H^+ ions increases the intensity of the yellow-green emissions because of the production of H-acceptors (H_{Zn}) [77, 78]. Violet emissions within the 430 nm to 450 nm range were observed in all the films [79]. The irradiation of H^+ to the lattice of ZnO induces the H_{Zn} (acceptor) shown by the appearance of a shoulder peak at 432 nm, ascribed to the recombination of donor-acceptor pairs, which is demonstrated by the shoulder peak [80]. It was observed that PL peaks moved slightly towards the lower wavelength indicating a decrease in oxygen vacancies that can be ascribed because of substitution of H^+ acceptor with Zn in the ZnO structure [81]. These peaks may be associated with intrinsic defects in the ZnO lattice or those induced by H^+ implantation, such as zinc and oxygen interstitials (Z_{ni} & O_i), oxygen vacancies (V_O), zinc vacancies (V_{Zn}), and among others [82, 83]. The intensity of emission peaks significantly decreased when H^+-ions were implanted in the lattice (ZnO), indicating a reduction in the recombination rate, enhanced charge separations, and improved charge-carrier mobility, ultimately benefiting the performance of FDSSCs.

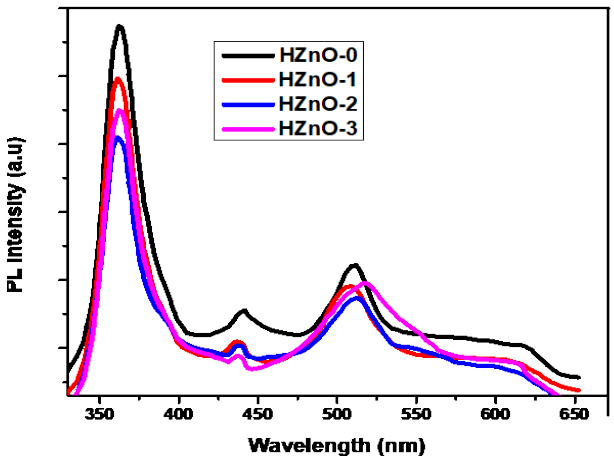

Fig. 7. PL spectra of unimplanted and HZnOs films.

3.6. JV characteristics

The current-density vs. voltage (J-V) characteristics of FDSSCs with N719 dye, as depicted in Figure 7, are accompanied by the corresponding photovoltaic properties listed in Table 3. The characterization of the FDSSCs relies on essential optimized photovoltaic parameters, including fill factor (FF) [84], open circuit voltage (V_{oc}) [85], short circuit current density (J_{sc})

[79], and photovoltaic conversion efficiency (η) [80] that can be determined by the methods outlined below:-

$$V_{oc} = |E_F - E_{redox}| \tag{19}$$

$$FF = \frac{I_{max} \times V_{max}}{J_{Sc} \times V_{oc}} \tag{20}$$

$$\eta = \frac{FF \times V_{oc} \times J_{sc}}{p_{in}} \tag{21}$$

The Fermi energy level (E_F), redox energy level (E_{redox}) of the electrolyte (I^-/I_3^-), maximum current (I_{max}), maximum voltage (V_{max}), and input power of the incident light (P_{in}) are the notations essential for characterizing and analyzing the device's performance under investigation.

Increasing FF improves the efficiency of FDSSCs by maximizing power conversion from incident light. The J_{sc} is measured when the device is short-circuited, and its higher value signifies the improved photon absorption and conversion to electrical current, leading to increased power output in FDSSCs. The V_{oc} is the difference between redox potential (electrolyte) and conduction band (semiconductor), and its higher values enable greater voltage generation and improved electrical potential. Optimizing the V_{oc} enhances FDSSCs efficiency by increasing maximum power output [62, 85].

The performance of unimplanted and H^+-implanted ZnO photoanodes in FDSSCs with N719 dye was evaluated. The unimplanted ZnO photoanodes exhibited J_{sc} (4.24 mA/cm^2), V_{oc} (0.74 V), I_m (3.64 A), V_m (0.60 V), and η (1.88%). However, the H^+-implanted ZnO photoanodes demonstrated superior photovoltaic properties compared to unimplanted ZnO film, indicated by improved J_{sc}, FF, and overall efficiency. The PCE of H^+-(1×10^{13}) ZnO film increased from 1.18% to 2.23%, while H^+-(1×10^{14}) ZnO exhibited an exceptional PCE of 2.47%. These improvements can be attributed to the effects of H^+ ion implantation, including a decrease in bandgap energy leading to an increased current density. The PL spectra revealed reduced peaks, indicating reduced charge carrier recombination [86]. Furthermore, introducing H^+ ions through ion implantation transformed the surface of the ZnO film into a porous structure, enhancing dye loading, light harvesting, and charge carrier densities.

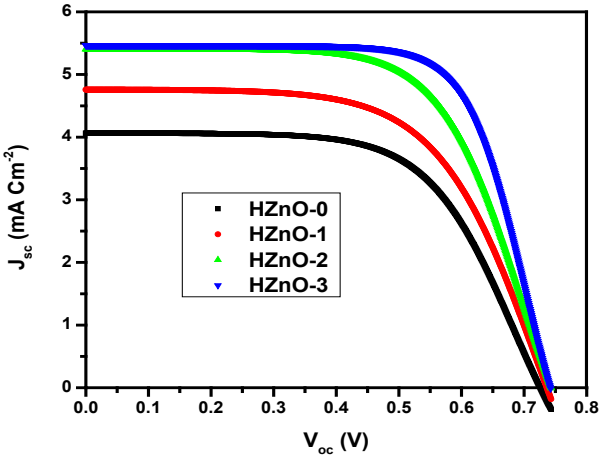

Fig. 8. The J-V Characteristics of all the samples.

The H^+-(1×10^{14}) ZnO film exhibits superior dye adsorption capacity compared to other photoanodes. Enabling H^+ ions into the ZnO films reduces the resistance associated with charge transfer at the interface (ZnO/electrolyte). This reduction in resistance led to faster electron transfer and decreased charge recombination rates, ultimately contributing to the enhanced efficiency of FDSSCs [87]. Furthermore, the H^+ ions implantation suppresses the development of

Zinc-dye complexes in the films, resulting in improved electronic injection efficiency of the semiconductor and increased efficiency of FDSSCs [42, 88]. In contrast to unimplanted ZnO-based photoanodes with low photocurrent response, the H^+-implanted ZnO photoanodes demonstrate significant photocurrent response, indicating an improved interfacial electron injection efficacy.

Introducing H^+ ions into ZnO photoanodes has proven effective in hindering the formation of Zn-dye complexes. Moreover, ZnO films have displayed instability when employed with acidic electrolytes. Nevertheless, the H^+ ions implantation into the ZnO film promotes the development of a corrosion-resistant interface, thereby enhancing the stability of FDSSCs. These modifications collectively contribute to the observed enhancement in overall efficiency.

Table 3. Photovoltaic parameters of all the FDSSCs.

Sample	J_{SC} ($mA.cm^{-2}$)	V_{OC} (V)	I_m (A)	V_m (V)	FF	η (%)
HZnO-0	4.2356	0.7446	3.6368	0.5186	0.5981	1.8862
HZnO-1	5.3986	0.7434	4.7925	0.5366	0.6407	2.5715
HZnO-2	5.4709	0.7431	5.0262	0.5701	0.7048	2.8652
HZnO-3	4.7713	0.7432	4.0775	0.5233	0.6017	2.1338

3.7. Electrochemical impedance spectroscopy (EIS)

The H^+-implantation effects on the charge transfer properties of the photoanode in the FDSSCs were examined using electrochemical impedance spectroscopy (EIS). Introducing H^+ ions during implantation can significantly influence the roughness and surface morphology of the ZnO films, consequently affecting charge transportation and species diffusion within the film. As illustrated in Figure 8, Nyquist plots were generated from EIS measurements to characterize the impedance behavior of the FDSSCs. The Nyquist plot comprises three distinct semi-circles, each shedding light on different aspects of the system. The intercept at the high frequency on the real axis of the Nyquist-plot can be attributed to the CE/electrolyte resistance (R_{pt}), representing the electrical resistance encountered at the interface of CE/electrolyte [89]. The larger semi-circle observed in the intermediate-frequency range is associated with the charge transfer resistance (R_{ct}) at the HZnO/Dye/Electrolyte interface [90], which elucidates the hindrance to charge transfer at the respective interfaces, providing valuable insights into charge transfer efficiency. Additionally, a smaller semi-circle in the lower-frequency region corresponds to the Warburg diffusion of the redox couple ($3I^-/I_3^-$) [91], revealing information regarding the conductivity of the ions and the diffusional properties of the electrolyte. Figure 8 demonstrates a decrease in the semi-circle or R_{ct} upon H^+ ion implantation in the ZnO film. The R_{ct} values exhibit a descending order of (HZnO-0) > (HZnO-1) > (HZnO-3) > (HZnO-2), with the HZnO-2 film implanted at a fluence of $1 \times 10^{14}\ ions/cm^2$ displaying the lowest R_{ct} across the HZnO/Dye/Electrolyte interface. This reduction in charge transfer resistance is indicative of a diminished recombination rate and enhanced fast electron transfer mobility, thus contributing to the highest efficiency in FDSSCs. Further investigation into the H^+-implantation effects on the FDSSCs performance is crucial for optimizing the charge transfer properties and advancing the overall efficiency of these solar cells.

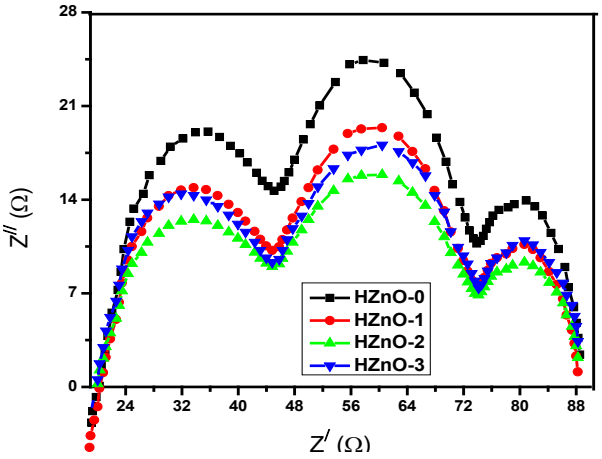

Fig. 9. Nyquist plot for unimplanted and H-implanted films.

4. Conclusion

ZnO films have been deposited on the ITO-PET by a spin coater. H^+ ions were then implanted in these films at fluencies 1×10^{13}, 1×10^{14}, and 1×10^{15} ions/cm^2. The H-implantation produced a p-type character in the ZnO films. The XRD patterns confirmed the irradiation of H^+ ions. It is observed that crystalline quality is degraded with decreased crystallite size. The least crystallite size is noticed at 1×10^{14} ions/cm^2. SRIM software reported that the amount of ionization and vacancies increases with the increase in ion dose. SEM analyzed the successful ions implantation of H^+ in the lattice of ZnO and reported that the surface of the ZnO became porous and rough. The H^+-irradiated films exhibited optical properties such as high absorbance, low bandgap energy (3.20 eV), narrowed bandgap edges, and high refractive index (2.29), particularly at a fluence 1×10^{14} ions/cm^2, because of the downward shifting of fermi level towards the valance band.

The cell developed by ZnO-2 film implanted at fluency 1×10^{14} ions/cm^2 indicated a high J_{sc} (5.4709 mA-cm^{-2}), FF (0.7048), and PCE (2.86%). EIS spectra reported that the charge transfer resistance (R_{ct}) decreases after H^+-ions implantation, especially at 1×10^{14} ions/cm^2 fluence. The H^+ ions implantation in the lattice of ZnO has been observed to reduce the rate of recombination, inhibit the formation of Zn^{2+}-dye composites, and enhance the charge carriers' concentration in photoanodes, resulting in the high efficiency of FDSSCs.

Funding

Researchers supporting project number (RSPD2024R741), King Saud University.

Acknowledgement

The authors would like to thank the Researchers Supporting Project number (RSPD2024R741), King Saud University, Riyadh, Saudi Arabia.

References

[1] Kutraleeswaran, M., et al., Dye sensitized Solar Cells,-A Review. J. Adv. Res. Appl. Sci, 2017. 4: p. 26-38.

[2] Myong, S.Y., K.S. Lim, Journal of crystal growth, 2006. 293(2): p. 253-257;

https://doi.org/10.1016/j.jcrysgro.2006.05.055
[3] Abdu, Y., M.K. Mustafa, M.K. Ahmad, British Journal of Physics Studies, 2022. 1(1): p. 27-39; https://doi.org/10.32996/bjps.2022.1.1.5
[https://www.tandfonline.com/doi/full/10.1080/19476337.2018.1518343, #64] Hosseinnezhad, M., Z. Ranjbar, Pigment & Resin Technology, 2023. 52(3): p. 310-320; https://doi.org/10.1108/PRT-01-2022-0010
[https://www.tandfonline.com/doi/full/10.1080/19476337.2018.1518343, #64] Kumar, P.N., et al., AIP Conference Proceedings. 2023. AIP Publishing; https://doi.org/10.1063/5.0140748
[6] Anand, A., et al., Materials Today: Proceedings, 2023. 72: p. 227-231; https://doi.org/10.1016/j.matpr.2022.07.048
[7] Yeoh, M.-E., et al., Materials Letters, 2023: p. 134730; https://doi.org/10.1016/j.matlet.2023.134730
[8] Rotte, N.K., et al., Journal of Physics and Chemistry of Solids, 2023. 174: p. 111175; https://doi.org/10.1016/j.jpcs.2022.111175
[https://www.tandfonline.com/doi/full/10.1080/19476337.2018.1518343, #64] Aksoy, S., et al., Physica E: Low-dimensional Systems and Nanostructures, 2020. 121: p. 114127; https://doi.org/10.1016/j.physe.2020.114127
[https://www.tandfonline.com/doi/full/10.1080/19476337.2018.1518343, #64] Savari, R., et al., Ceramics International, 2021. 47(22): p. 31927-31939; https://doi.org/10.1016/j.ceramint.2021.08.079
[11] Kumar, V., et al., Chemical Engineering Journal Advances, 2023. 15: p. 100501; https://doi.org/10.1016/j.ceja.2023.100501
[12] Akcan, D., A. Gungor, L. Arda, Journal of Molecular structure, 2018. 1161: p. 299-305; https://doi.org/10.1016/j.molstruc.2018.02.058
[13] Ahmad, M.S., A.K. Pandey, N. Abd Rahim, Renewable and Sustainable Energy Reviews, 2017. 77: p. 89-108; https://doi.org/10.1016/j.rser.2017.03.129
[14] Kumar, P., et al., RSC advances, 2017. 7(15): p. 9160-9168; https://doi.org/10.1039/C6RA17069B
[https://www.tandfonline.com/doi/full/10.1080/19476337.2018.1518343, #64] Krishna, R., D.C. Agarwal, D.K. Avasthi, Radiation Effects and Defects in Solids, 2021. 176(1-2): p. 145-166; https://doi.org/10.1080/10420150.2021.1891065
[16] Kumar, P., et al., Applied Surface Science, 2018. 452: p. 217-222; https://doi.org/10.1016/j.apsusc.2018.04.263
[17] Jayanthi, K., et al., Applied Surface Science, 2009. 255(11): p. 5869-5875; https://doi.org/10.1016/j.apsusc.2009.01.032
[18] Yao, B., et al., Journal of Physics D: Applied Physics, 2008. 42(1): p. 015407; https://doi.org/10.1088/0022-3727/42/1/015407
[https://www.tandfonline.com/doi/full/10.1080/19476337.2018.1518343, #64] Janotti, A., C.G. Van de Walle, Reports on progress in physics, 2009. 72(12): p. 126501; https://doi.org/10.1088/0034-4885/72/12/126501
[https://www.tandfonline.com/doi/full/10.1080/19476337.2018.1518343, #64] Shohany, B.G., A.K. Zak, Ceramics International, 2020. 46(5): p. 5507-5520; https://doi.org/10.1016/j.ceramint.2019.11.051
[21] Van de Walle, C.G., Physical review letters, 2000. 85(5): p. 1012; https://doi.org/10.1103/PhysRevLett.85.1012
[22] Kim, C.Y., J.H. Park, T.G. Kim, Journal of Alloys and Compounds, 2018. 732: p. 300-305; https://doi.org/10.1016/j.jallcom.2017.10.217
[https://www.ncbi.nlm.nih.gov/pmc/articles/PMC7182362/, #65] Van Hoang, D., et al., Journal of Materiomics, 2022. 8(1): p. 123-135; https://doi.org/10.1016/j.jmat.2021.04.011

[24] Tsay, C.-Y., et al., Materials Science in Semiconductor Processing, 2021. 121: p. 105295; https://doi.org/10.1016/j.mssp.2020.105295

[25] Bhattacharjee, R., I.-M. Hung, Materials Chemistry and Physics, 2014. 143(2): p. 693-701; https://doi.org/10.1016/j.matchemphys.2013.09.055

[26] Yousefi, R., A.K. Zak, F. Jamali-Sheini, Ceramics International, 2013. 39(2): p. 1371-1377; https://doi.org/10.1016/j.ceramint.2012.07.076

[27] Herng, T., et al., Applied physics letters, 2007. 90(3): p. 032509; https://doi.org/10.1063/1.2433028

[28] Tyona, M., et al., Adv. Appl. Sci. Res, 2015. 6: p. 7-20.

[29] Yi, J., et al., Physical review letters, 2010. 104(13): p. 137201; https://doi.org/10.1103/PhysRevLett.104.137201

[30] Das, A., P. Malakar, R.G. Nair, Materials Letters, 2018. 219: p. 76-80; https://doi.org/10.1016/j.matlet.2018.02.057

[31] Zhang, J., et al., Materials Research Bulletin, 2015. 65: p. 7-13; https://doi.org/10.1016/j.materresbull.2015.01.004

[32] Tyona, M., IntechOpen London, United Kingdom.

[https://www.tandfonline.com/doi/full/10.1080/19476337.2018.1518343, #64] Das, A., R.R. Wary, R.G. Nair, Solid State Sciences, 2020. 104: p. 106290; https://doi.org/10.1016/j.solidstatesciences.2020.106290

[https://www.tandfonline.com/doi/full/10.1080/19476337.2018.1518343, #64] Kadam, A., et al., Journal of Alloys and Compounds, 2017. 710: p. 102-113; https://doi.org/10.1016/j.jallcom.2017.03.150

[35] Ahmad, M., et al., Applied surface science, 2013. 285: p. 702-712; https://doi.org/10.1016/j.apsusc.2013.08.114

[https://www.ncbi.nlm.nih.gov/pmc/articles/PMC7182362/, #65] Rajasekaran, M., A. Arunachalam, P. Kumaresan, Materials Research Express, 2020. 7(3): p. 036412; https://doi.org/10.1088/2053-1591/ab815d

[https://www.tandfonline.com/doi/full/10.1080/19476337.2018.1518343, #64] Yilmaz, M., G. Turgut, Kovove Mater, 2015. 53(5): p. 333-339; https://doi.org/10.4149/m_2015_5_333

[38] Mehmood, B., et al., International Journal of Energy Research, 2020; https://doi.org/10.1002/er.5939

[39] Tsay, C.-Y., et al., Thin Solid Films, 2009. 518(5): p. 1603-1606; https://doi.org/10.1016/j.tsf.2009.09.054

[40] Ali, S.O., et al., Advanced Energy Conversion Materials, 2021: p. 27-44; https://doi.org/10.37256/aecm.222021802

[41] Zhuang, S., et al., Electrochimica Acta, 2019. 294: p. 28-37; https://doi.org/10.1016/j.electacta.2018.10.045

[42] Vasudev, R.A., Synthesis and characterization of nanocrystalline ZnO Gas Sensor. 2015.

[https://www.tandfonline.com/doi/full/10.1080/19476337.2018.1518343, #64] Liu, J., et al., Superlattices and Microstructures, 2012. 52(4): p. 765-773; https://doi.org/10.1016/j.spmi.2012.06.021

[44] Verma, H.K., M. Vij, K. Maurya, Journal of Nanoscience and Nanotechnology, 2020. 20(6): p. 3683-3692; https://doi.org/10.1166/jnn.2020.17679

[45] Pawar, R.C., et al., Materials Chemistry and Physics, 2015. 151: p. 167-180; https://doi.org/10.1016/j.matchemphys.2014.11.051

[46] Thangavel, R., et al., Journal of Raman Spectroscopy, 2010. 41(12): p. 1594-1600; https://doi.org/10.1002/jrs.2599

[https://www.tandfonline.com/doi/full/10.1080/19476337.2018.1518343, #64] Bouloudenine, M., et al., Catalysis today, 2006. 113(3-4): p. 240-244; https://doi.org/10.1016/j.cattod.2005.11.073

[48] Bhagwat, U.O., et al., Journal of Photochemistry and Photobiology A: Chemistry, 2017. 346: p. 559-569; https://doi.org/10.1016/j.jphotochem.2017.06.043

[49] Zamiri, R., et al., Physical Chemistry Chemical Physics, 2014. 16(40): p. 22418-22425; https://doi.org/10.1039/C4CP02945C

[50] Mia, M.N.H., et al., Results in physics, 2017. 7: p. 2683-2691; https://doi.org/10.1016/j.rinp.2017.07.047

[https://www.tandfonline.com/doi/full/10.1080/19476337.2018.1518343, #64] Arif, M., et al., Optics & Laser Technology, 2019. 112: p. 539-547; https://doi.org/10.1016/j.optlastec.2018.11.006

[52] Devi, P.G., A.S. Velu, Journal of Theoretical and Applied Physics, 2016. 10(3): p. 233-240; https://doi.org/10.1007/s40094-016-0221-0

[53] Khan, M.F., et al., Nuclear Instruments and Methods in Physics Research Section B: Beam Interactions with Materials and Atoms, 2016. 368: p. 45-49; https://doi.org/10.1016/j.nimb.2015.12.010

[54] Natu, K., V.K. Kaushik, M. Laad, Journal of the Korean Physical Society, 2023: p. 1-9; https://doi.org/10.1007/s40042-023-00809-7

[55] Pal, J., et al., The Journal of Physical Chemistry C, 2015. 119(7): p. 3780-3790; https://doi.org/10.1021/jp5114812

[56] Herve, P., L. Vandamme, Infrared physics & technology, 1994. 35(4): p. 609-615; https://doi.org/10.1016/1350-4495(94)90026-4

[57] Shan, F., et al., Transparent conductive ZnO thin films on glass substrates deposited by pulsed laser deposition. 2005. 277(1-4): p. 284-292; https://doi.org/10.1016/j.jcrysgro.2005.01.016

[58] Khan, M., et al., Optical Materials, 2021. 122: p. 111610; https://doi.org/10.1016/j.optmat.2021.111610

[59] Hwang, Y., et al., Materials Research Bulletin, 2012. 47(10): p. 2898-2901; https://doi.org/10.1016/j.materresbull.2012.04.111

[60] Xue, S., et al., Physica B: Condensed Matter, 2006. 381(1-2): p. 209-213; https://doi.org/10.1016/j.physb.2006.01.342

[61] Khan, M., et al., Ceramics International, 2023.

[https://www.ncbi.nlm.nih.gov/pmc/articles/PMC7182362/, #65] Bahadur, A., M. Mishra, Acta Phys. Pol. A, 2013. 123(4): p. 737-740; https://doi.org/10.12693/APhysPolA.123.737

[https://www.tandfonline.com/doi/full/10.1080/19476337.2018.1518343, #64] Aydin, C., Journal of Alloys and Compounds, 2019. 777: p. 145-151; https://doi.org/10.1016/j.jallcom.2018.10.325

[64] Alias, M., K.M. Rashid, K. Adem, International Journal of Innovative Research in Science, Engineering and Technology, 2014. 3(8): p. 15538-15544; https://doi.org/10.15680/IJIRSET.2014.0308064

[65] Kahouli, M., et al., Superlattices and Microstructures, 2015. 85: p. 7-23; https://doi.org/10.1016/j.spmi.2015.05.007

[66] Bouaziz, L., et al., Materials Today Communications, 2022. 31: p. 103450; https://doi.org/10.1016/j.mtcomm.2022.103450

[67] https://www.tandfonline.com/doi/full/ 10.1080/19476337.2018.1518343.

[68] https://www.ncbi.nlm.nih.gov/pmc/articles/PMC7182362/

[69] Boukhachem, A., et al., Materials Science in Semiconductor Processing, 2012. 15(3): p. 282-292; https://doi.org/10.1016/j.mssp.2012.02.014

[70] Xie, G., et al., Physics Procedia, 2012. 32: p. 651-657; https://doi.org/10.1016/j.phpro.2012.03.614

[https://www.ncbi.nlm.nih.gov/pmc/articles/PMC7182362/, #65] Xu, Y., M.A. Schoonen, American Mineralogist, 2000. 85(3-4): p. 543-556; https://doi.org/10.2138/am-2000-0416

[72] Nakagawa, T., et al., Nuclear Instruments and Methods in Physics Research Section B: Beam Interactions with Materials and Atoms, 2005. 232(1-4): p. 343-347;
https://doi.org/10.1016/j.nimb.2005.03.070

[73] Rahmati, A., et al., The European Physical Journal Plus, 2014. 129(11): p. 1-7;
https://doi.org/10.1140/epjp/i2014-14250-8

[74] Moussawi, R.N., D. Patra, RSC advances, 2016. 6(21): p. 17256-17268;
https://doi.org/10.1039/C5RA20221C

[75] Ren, C., et al., Journal of hazardous materials, 2010. 182(1-3): p. 123-129;
https://doi.org/10.1016/j.jhazmat.2010.05.141

[https://www.tandfonline.com/doi/full/10.1080/19476337.2018.1518343, #64] Xu, X., et al., The Journal of Physical Chemistry C, 2012. 116(15): p. 8813-8818; https://doi.org/10.1021/jp3014749

[77] Rauch, C., et al., Journal of Applied Physics, 2010. 107(2);
https://doi.org/10.1063/1.3275889

[78] Dejam, L., et al., ZnO, Results in Physics, 2023. 44: p. 106209;
https://doi.org/10.1016/j.rinp.2023.106209

[79] Ferreyra, J.M., et al., Solid State Communications, 2017. 257: p. 42-46;
https://doi.org/10.1016/j.ssc.2017.04.002

[https://www.tandfonline.com/doi/full/10.1080/19476337.2018.1518343, #64] Studenikin, S., N. Golego, M. Cocivera, Journal of Applied physics, 1998. 84(4): p. 2287-2294;
https://doi.org/10.1063/1.368295

[81] Zhang, X., A. Wang, M. ZhaoCarbon, 2015. 84: p. 1-8;
https://doi.org/10.1016/j.carbon.2014.11.049

[https://www.ncbi.nlm.nih.gov/pmc/articles/PMC7182362/, #65] Xie, W., et al., Journal of Photochemistry and Photobiology A: chemistry, 2010. 216(2-3): p. 149-155;
https://doi.org/10.1016/j.jphotochem.2010.06.032

[https://www.tandfonline.com/doi/full/10.1080/19476337.2018.1518343, #64] Singh, S., A. Singh, N. Kaur, J Mater, 2016. 2016: p. 1-11;
https://doi.org/10.1155/2016/9081346

[84] Khan, M., et al., Journal of Nanoelectronics and Optoelectronics, 2019. 14(11): p. 1582-1588;
https://doi.org/10.1166/jno.2019.2535

[85] Chen, Y.-C., et al., Journal of Alloys and Compounds, 2022. 899: p. 163348;
https://doi.org/10.1016/j.jallcom.2021.163348

[86] Aneesiya, K.R., C. Louis, Journal of Alloys and Compounds, 2020. 829: p. 154497;
https://doi.org/10.1016/j.jallcom.2020.154497

[87] Sudhagar, P., et al., Materials Research Bulletin, 2011. 46(9): p. 1473-1479;
https://doi.org/10.1016/j.materresbull.2011.04.027

[88] Koide, N., et al., Journal of Photochemistry and Photobiology A: chemistry, 2006. 182(3): p. 296-305;
https://doi.org/10.1016/j.jphotochem.2006.04.030

[89] Rajan, A.K., L. Cindrella, Materials Research Express, 2019. 6(8): p. 0850e6;
https://doi.org/10.1088/2053-1591/ab2698

[90] Zhu, G., et al., Journal of Materials Chemistry, 2012. 22(46): p. 24326-24329;
https://doi.org/10.1039/c2jm33219a